Online Supplement for "Poiseuille flow of a Bingham fluid in a channel with a superhydrophobic groovy wall"

This online supplement is structured into six sections, as follows.

1. Approximate model

Certain flow assumptions may allow us to develop an approximate solution for creeping flow of the thick channel limit, which we develop for the sake of completeness of the current study. In solving equation (3.5) of the manuscript, the term $dU_0/dy = C_1+2C_2y$, which is generally a function of y, can be approximated with a constant value for the range of thick channels. In this range, the wall-induced perturbations occur in a near wall region and they decay in the normal direction to the wall (*i.e.* the y direction). To be clear, if we consider that the height of the near wall region containing the perturbation field is y_p, therefore, for thick channels where $y_p \ll 1$, the no-slip flow gradient ($dU_0/dy = C_1+2C_2y$) reduces to $dU_0/dy \approx C_1$, since the term $2C_2y$ (for $y \leqslant y_p$) becomes small compared to C_1. Therefore, we use the approximation of $dU_0/dy \approx C_1$, where C_1 is the no-slip velocity gradient at the lower wall and it always has a positive real value. Consequently, equation (3.5) of the manuscript is reduced to an ordinary differential equation with constant coefficients. For a Bingham fluid ($Bi \neq 0$), when $n \neq 0$, the following exponential solution is expected:

$$\hat{\psi} = A_n e^{\lambda_n^{(1)} y} + B_n e^{\lambda_n^{(2)} y} + C_n e^{\lambda_n^{(3)} y} + D_n e^{\lambda_n^{(4)} y}, \tag{S1}$$

where $\lambda_n^{(1)}$, $\lambda_n^{(2)}$, $\lambda_n^{(3)}$ and $\lambda_n^{(4)}$ are the four distinct roots of the following characteristic equation:

$$\lambda_n^4 - \left(2 + \frac{4Bi}{C_1}\right) n^2\kappa^2\lambda_n^2 + 8Bi\frac{C_2}{C_1^2} n^2\kappa^2\lambda_n + n^4\kappa^4 = 0. \tag{S2}$$

For $n = 0$, the previously obtained quadratic function solution is valid. Therefore, the solution for the perturbation stream function and velocities are written as:

$$\psi(x,y) = J_0 + E_0 y + F_0 y^2 + \sum_{n=1}^{\infty} \zeta_n^{(\mathrm{I})} \cos(n\kappa x), \tag{S3}$$

$$u(x,y) = E_0 + 2F_0 y + \sum_{n=1}^{\infty} \zeta_n^{(\mathrm{II})} \cos(n\kappa x), \tag{S4}$$

$$v(x,y) = \sum_{n=1}^{\infty} n\kappa \zeta_n^{(\mathrm{I})} \sin(n\kappa x), \tag{S5}$$

where $\zeta_n^{(\mathrm{I})}$ and $\zeta_n^{(\mathrm{II})}$ are:

$$\begin{cases} \zeta_n^{(\mathrm{I})} = A_n e^{\lambda_n^{(1)} y} + B_n e^{\lambda_n^{(2)} y} + C_n e^{\lambda_n^{(3)} y} + D_n e^{\lambda_n^{(4)} y}, \\ \zeta_n^{(\mathrm{II})} = A_n \lambda_n^{(1)} e^{\lambda_n^{(1)} y} + B_n \lambda_n^{(2)} e^{\lambda_n^{(2)} y} + C_n \lambda_n^{(3)} e^{\lambda_n^{(3)} y} + D_n \lambda_n^{(4)} e^{\lambda_n^{(4)} y}. \end{cases} \tag{S6}$$

For the boundary conditions, we again consider $\psi = 0$ at the SH wall (no-penetration condition) and zero perturbation velocities at the lower yield surface; thus, we find:

$$\psi(x,0) = 0, \qquad v(x,h) = 0, \qquad u(x,h) = 0. \tag{S7}$$

Applying the above-mentioned boundary conditions, we obtain:

$$\begin{cases} J_0 = 0, \\ F_0 = -\frac{E_0}{2h}, \\ B_n = C_B A_n, \\ C_n = C_C A_n, \\ D_n = C_D A_n, \end{cases} \tag{S8}$$

where the coefficients C_B, C_C, C_D are found as:

$$\begin{cases} C_B = -\dfrac{\left(\lambda_n^{(3)}-\lambda_n^{(4)}\right)e^{\left(\lambda_n^{(3)}+\lambda_n^{(4)}\right)h}+\left(\lambda_n^{(1)}-\lambda_n^{(3)}\right)e^{\left(\lambda_n^{(1)}+\lambda_n^{(3)}\right)h}+\left(\lambda_n^{(4)}-\lambda_n^{(1)}\right)e^{\left(\lambda_n^{(1)}+\lambda_n^{(4)}\right)h}}{\left(\lambda_n^{(2)}-\lambda_n^{(3)}\right)e^{\left(\lambda_n^{(2)}+\lambda_n^{(3)}\right)h}+\left(\lambda_n^{(4)}-\lambda_n^{(2)}\right)e^{\left(\lambda_n^{(2)}+\lambda_n^{(4)}\right)h}+\left(\lambda_n^{(3)}-\lambda_n^{(4)}\right)e^{\left(\lambda_n^{(3)}+\lambda_n^{(4)}\right)h}}, \\ C_C = \dfrac{\left(\lambda_n^{(2)}-\lambda_n^{(4)}\right)e^{\left(\lambda_n^{(2)}+\lambda_n^{(4)}\right)h}+\left(\lambda_n^{(1)}-\lambda_n^{(2)}\right)e^{\left(\lambda_n^{(1)}+\lambda_n^{(2)}\right)h}+\left(\lambda_n^{(4)}-\lambda_n^{(1)}\right)e^{\left(\lambda_n^{(1)}+\lambda_n^{(4)}\right)h}}{\left(\lambda_n^{(2)}-\lambda_n^{(3)}\right)e^{\left(\lambda_n^{(2)}+\lambda_n^{(3)}\right)h}+\left(\lambda_n^{(4)}-\lambda_n^{(2)}\right)e^{\left(\lambda_n^{(2)}+\lambda_n^{(4)}\right)h}+\left(\lambda_n^{(3)}-\lambda_n^{(4)}\right)e^{\left(\lambda_n^{(3)}+\lambda_n^{(4)}\right)h}}, \\ C_D = -\dfrac{\left(\lambda_n^{(2)}-\lambda_n^{(3)}\right)e^{\left(\lambda_n^{(2)}+\lambda_n^{(3)}\right)h}+\left(\lambda_n^{(1)}-\lambda_n^{(2)}\right)e^{\left(\lambda_n^{(1)}+\lambda_n^{(2)}\right)h}+\left(\lambda_n^{(3)}-\lambda_n^{(1)}\right)e^{\left(\lambda_n^{(1)}+\lambda_n^{(3)}\right)h}}{\left(\lambda_n^{(2)}-\lambda_n^{(3)}\right)e^{\left(\lambda_n^{(2)}+\lambda_n^{(3)}\right)h}+\left(\lambda_n^{(4)}-\lambda_n^{(2)}\right)e^{\left(\lambda_n^{(2)}+\lambda_n^{(4)}\right)h}+\left(\lambda_n^{(3)}-\lambda_n^{(4)}\right)e^{\left(\lambda_n^{(3)}+\lambda_n^{(4)}\right)h}}. \end{cases} \tag{S9}$$

Considering $E_0 = A_0$ and substituting equation (S8) into equations (S3)-(S5), the following solutions are obtained:

$$\psi(x,y) = A_0\left(y - \frac{y^2}{2h}\right) + \sum_{n=1}^{\infty} A_n \zeta_n^{(\mathrm{III})} \cos\left(n\kappa x\right), \tag{S10}$$

$$u(x,y) = A_0\left(1 - \frac{y}{h}\right) + \sum_{n=1}^{\infty} A_n \zeta_n^{(\mathrm{IV})} \cos\left(n\kappa x\right), \tag{S11}$$

$$v(x,y) = \sum_{n=1}^{\infty} A_n n\kappa \zeta_n^{(\mathrm{III})} \sin\left(n\kappa x\right), \tag{S12}$$

where

$$\begin{cases} \zeta_n^{(\mathrm{III})} = e^{\lambda_n^{(1)} y} + C_B e^{\lambda_n^{(2)} y} + C_C e^{\lambda_n^{(3)} y} + C_D e^{\lambda_n^{(4)} y}, \\ \zeta_n^{(\mathrm{IV})} = \lambda_n^{(1)} e^{\lambda_n^{(1)} y} + C_B \lambda_n^{(2)} e^{\lambda_n^{(2)} y} + C_C \lambda_n^{(3)} e^{\lambda_n^{(3)} y} + C_D \lambda_n^{(4)} e^{\lambda_n^{(4)} y}. \end{cases} \tag{S13}$$

To find the unknown coefficients A_n in above solutions, we employ the slip and no-slip boundary conditions at the SH wall and follow the same method developed in the semi-analytical model section. Consequently, we have a system of linear algebraic equations that is solved numerically for the unknown coefficients A_n. The iterative approach discussed earlier is then followed to capture the location of the lower yield surface. Since the approximate solution only includes linear algebraic equations, it is easy-to-implement, fast, and robust. For a more detailed analysis, we evaluate the accuracy of the approximate solution, by comparing its results to those of the full semi-analytical solution. To make the comparison, we consider a thick channel with $\ell = 0.2$ and $\varphi = 0.5$. The flow is creeping, the Bingham numbers are chosen as $Bi = 1$ and $Bi = 10$, and the slip numbers are relatively large (there is no plug formation at the SH wall). As shown in Figure S1, an excellent agreement between the semi-analytical and approximate model results is found, confirming the accuracy of the approximate solution for the creeping flow in the thick channel limit.

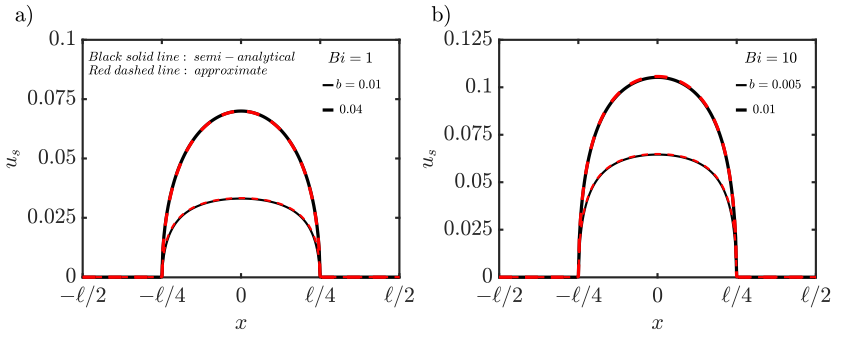

FIGURE S1. Comparison between the semi-analytical and approximate model results. The slip velocity for a thick channel with $\ell = 0.2$ and $\varphi = 0.5$. The flow is creeping.

2. Evaluation of the order of the inertial terms

Keeping the non-linear advection terms and rewriting equation (3.19) of the manuscript using the perturbation parameter $\epsilon = \kappa^{-1}$, we obtain the following equation:

$$Re\left[\overbrace{U_0\left(\frac{\partial^3\psi}{\partial x\partial y^2}+\frac{\partial^3\psi}{\partial x^3}\right)\kappa^{-1}}^{(1)}\overbrace{-\left(d^2U_0/dy^2\right)\frac{\partial\psi}{\partial x}\kappa^{-1}}^{(2)}+\overbrace{\frac{\partial\psi}{\partial y}\left(\frac{\partial^3\psi}{\partial x\partial y^2}+\frac{\partial^3\psi}{\partial x^3}\right)\kappa^{-2}}^{(3)}\overbrace{-\frac{\partial\psi}{\partial x}\left(\frac{\partial^3\psi}{\partial x^2\partial y}+\frac{\partial^3\psi}{\partial y^3}\right)\kappa^{-2}}^{(4)}\right]= \tag{S14}$$

$$\left[\begin{array}{l}\frac{\partial^4\psi}{\partial x^4}+\frac{\partial^4\psi}{\partial y^4}+\left(2+\frac{4Bi}{|dU_0/dy|}\right)\frac{\partial^4\psi}{\partial x^2\partial y^2}-\\ 4Bi\frac{d^2U_0/dy^2}{(dU_0/dy)^2}\frac{\partial^3\psi}{\partial x^2\partial y}\end{array}\right]\kappa^{-1}+O(\kappa^{-2}).$$

where the inertial terms are numbered from 1 to 4, while the third and fourth terms represent the non-linear advection terms. For the thick channel limit, we can re-scale equation (S14) using $X = \kappa x$, $Y = \kappa y$ and $\Psi = \kappa\psi$, where $X-Y$ is the scaled coordinate system and Ψ is the scaled perturbation stream function. This scaling originates from the fact that the perturbation field becomes negligible when reaching a distance from the SH wall (in the y direction) which is within the same magnitude order as the groove periodicity length. In the new coordinate system, X and Y are of $O(1)$ since the upper bound in Y where the perturbation field becomes negligible is of order one. Therefore,

equation (S14) can be rewritten, after simplifications, in the following form:

$$Re\left[\overbrace{U_0\left(\frac{\partial^3\Psi}{\partial X\partial Y^2}+\frac{\partial^3\Psi}{\partial X^3}\right)\kappa^{-2}}^{(1)}\overbrace{-\left(d^2U_0/dy^2\right)\frac{\partial\Psi}{\partial X}\kappa^{-4}}^{(2)}+\overbrace{\frac{\partial\Psi}{\partial Y}\left(\frac{\partial^3\Psi}{\partial X\partial Y^2}+\frac{\partial^3\Psi}{\partial X^3}\right)\kappa^{-3}}^{(3)}-\overbrace{\frac{\partial\Psi}{\partial X}\left(\frac{\partial^3\Psi}{\partial X^2\partial Y}+\frac{\partial^3\Psi}{\partial Y^3}\right)\kappa^{-3}}^{(4)}\right]= \tag{S15}$$

$$\left[\begin{array}{l}\left\{\frac{\partial^4\Psi}{\partial X^4}+\frac{\partial^4\Psi}{\partial Y^4}+\left(2+\frac{4Bi}{|dU_0/dy|}\right)\frac{\partial^4\Psi}{\partial X^2\partial Y^2}\right\}\kappa^{-1}- \\ 4Bi\frac{d^2U_0/dy^2}{(dU_0/dy)^2}\frac{\partial^3\Psi}{\partial X^2\partial Y}\kappa^{-2}\end{array}\right]+O(\kappa^{-3}).$$

For $Re=\kappa$, the first advection term (term 1) in equation (S15) has the same order of magnitude as the first three viscous terms. Note that for $\ell=0.2$, which in our work is the common value of ℓ presented in several figures, we have $\kappa\approx 31$. For $Re=\kappa^2$, the non-linear inertial terms (terms 3 and 4) become comparable to the viscous terms, thus, affecting the flow. Therefore, for $\ell=0.2$, we may expect that for $Re\gtrsim 900$, the neglected non-linear terms could have an effect on the flow solution. However, one should note that the significance of such effects also depends on the slip number. For example, comparing the accuracy of the semi-analytical solutions in Figures 3 and 4 of the manuscript, one can realize that the increase in the slip number from $b=0.01$ to $b=0.04$ (for $Bi=1$) has a significant effect on the accuracy of the semi-analytical solution of the slip velocity, due to the growth of the non-linear advection terms. However, considering Figure 2 of the manuscript, even at $Re=3600$, overall, the semi-analytical solution still provides a reasonable accuracy for the large slip numbers taken.

3. Computational mesh

To generate the computational domain, we consider a portion of the channel that contains only one period of the SH groovy wall. Therefore, a periodic boundary condition is applied at the inlet and outlet, while the no-slip condition is dedicated for the upper wall and the no-slip regions of the SH lower wall. A linear Navier slip model is considered for the slip region of the SH wall, which is developed for OpenFOAM 2.2.x by Vasudevan (2017).

Due to the fact that we employ the DNS to simulate flow configurations with a wide range of Reynolds numbers, the size of the computational mesh is important. In other words, we seek highly resolved simulations in space. To ensure a sufficiently fine computational mesh, we follow the DNS standards. Knowing the fact that the lower yielded zone is perturbed about the no-slip Poiseuille flow, for our Bingham fluid, we define the friction velocity as:

$$\hat{u}_\tau=\sqrt{\hat{\nu}_p\frac{d\hat{U}_0}{d\hat{y}}+\frac{\hat{\tau}_0}{\hat{\rho}}}, \tag{S16}$$

where $\hat{\nu}_p$ is the plastic kinematic viscosity and $d\hat{U}_0/dy$ roughly represents the average velocity gradient at the SH wall. In this study, a non-uniform orthogonal mesh is used, such that a finer mesh size is considered for the near wall region compared to the channel center. Additional mesh refinement is considered for the regions close to the groove edges, *i.e.* the connecting points between the slip and no-slip regions at the SH wall

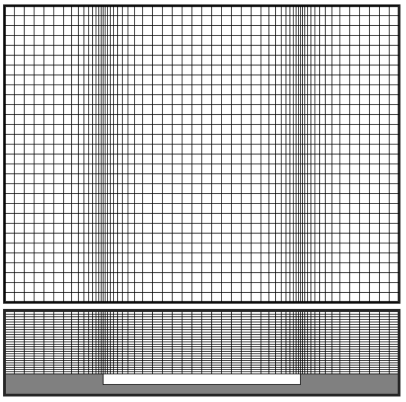

FIGURE S2. Computational mesh for the region close to the SH wall (lower panel, $0 \leqslant y \leqslant 0.03$) and the middle of the channel (upper panel, $0.92 \leqslant y \leqslant 1.07$), where $\ell = 0.2$, $\varphi = 0.5$ and $-\ell/2 \leqslant x \leqslant \ell/2$. The grey area illustrates the SH groovy wall where air is trapped inside the white area.

(see Figure S2). The simulations are typically carried out with the use of $N_x \times 600$, as the number of cells in the x and y directions, respectively. For the simulated channel of $\ell = 0.2$ (frequently presented in this study), the number of cells in the x direction is chosen as $N_x = 60$. The cell sizes corresponding to the selected mesh are consistent with the DNS requirements. For the most extreme case considered in this study, *i.e.* $\ell = 0.2$, $Re = 3600$ and $Bi = 10$ ($Re_\tau = \hat{u}_\tau \hat{H}/\hat{\nu}_p \approx 240$), our average cell sizes in the x and y directions are $\bar{\Delta}x^+, \bar{\Delta}y^+ \approx 0.8$, respectively (here the bar sign denotes the average value and the plus sign represents the normalized value with respect to the viscous wall unit, *i.e.* $\frac{\hat{\nu}_p}{\hat{u}_\tau}$). In addition, for this extreme case, the size of the cell adjacent to the wall is obtained as $y^+ \approx 0.24$. The selected computational mesh also provide us with accurate and converged values of the slip velocity and its gradients at the SH wall as well as the total velocity field.

It is worth mentioning that, for large Reynolds numbers, we have also conducted DNS simulations in a long channel with 10 grooves, without enforcing periodic conditions at the inlet and outlet boundaries. We have found that the results are similar to those of the periodic domain (Figure S2), confirming that, based on the assumptions made, the dominant flow period can be the same as that of the SH groovy wall for our flow (results omitted for brevity). However, as discussed previously, in general the flow period could differ from that of the flow geometry, which can be analyzed in future, *e.g.* via a stability analysis.

4. Evaluation of the regularization parameter ($\hat{m}$)

The effects of the Papanastasiou regularization parameter ($\hat{m}$) on our DNS velocity profiles are evaluated in Figure S3, where the slip and total velocity profiles for the creeping flow (at $Bi = 10$) are presented, based on considering three values of $\hat{m} = 10^3$ (s), $\hat{m} = 10^5$ (s) and $\hat{m} = 10^7$ (s). For larger regularization parameters, the physics of our viscoplastic fluid flow (especially the unyielded plug zone) can be captured more accurately, while the computations become more costly. For the sake of calculating the velocity profiles, Figure S3 shows that the DNS results with $\hat{m} = 10^3$ (s) are as accurate as those with larger values of $\hat{m}$, albeit converged faster. Therefore, in the present study, in calculating the velocity profiles, we have mainly relied on $\hat{m} = 10^3$ (s); however,

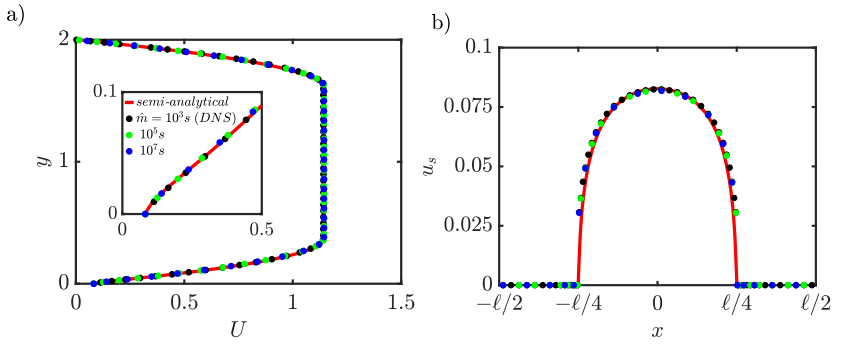

FIGURE S3. Semi-analytical and DNS results. Effects of the Papanastasiou regularization parameter ($\hat{m}$) on the results for $\ell = 0.2$, $\varphi = 0.5$, $Re = 0.01$, $Bi = 10$ and $b = 0.007$. a) Total streamwise velocity profile at $x = 0$. b) Slip velocity.

for other purposes such as capturing the plug zone formation at the SH wall, we have conducted simulations with $\hat{m} = 10^7$ (s), to have accurate predictions of the onsets of such a phenomenon.

5. Analysis of dimensional and dimensionless flow parameters from an experimental perspective

Here, let us briefly discuss about the possible/typical ranges of the dimensional and dimensionless parameters, useful for an experimental study in relation to our flow. Let us start from, in particular, the viscoplastic fluid's rheological properties, the typical structures of the SH surface, and the other flow parameters (*e.g.* the channel height and the average flow velocity), described as follows. (i) Regarding the fluid, these days, Carbopol gels are usually used as experimental viscoplastic materials, whose rheological properties depend on the concentration and acidity of Carbopol (Eslami & Taghavi 2019). This allows one to achieve a wide range of yield stress values. For instance, the measured yield stress values for relatively large Carbopol concentrations of 0.15% and 0.2% (wt/wt) have been reported as $\hat{\tau}_0 = 13.7$ (Pa) (Eslami & Taghavi 2019) and $\hat{\tau}_0 = 25.3$ (Pa) (Pourzahedi *et al.* 2021). Similar values have been reported in other works (Eslami & Taghavi 2017; Lyu & Taghavi 2020; Eslami *et al.* 2020, 2022; Akbari & Taghavi 2022*a*,*b*; Taghavi 2022). Therefore, the yield stress values of Carbopol gels can be as large as tens of Pascals; however, their densities are typically very close to that of water (Balmforth *et al.* 2014; Eslami & Taghavi 2019). In practice, a wide range of values for the plastic viscosity of experimental viscoplastic fluids can be also considered, *e.g.* $0.001 \leqslant \hat{\mu}_p \leqslant 0.1$ $(Pa.s)$. (ii) Regarding the SH geometry, a wide range of values have been reported for the groove width (*i.e.* the slip area width), depth and period. For example, Choi *et al.* (2021) have conducted flow experiments using groovy SH walls, with the groove width of $72-96$ (μm), the depth of $124-144$ (μm) and the period of ~ 200 (μm). Also, Mongruel *et al.* (2013) have used SH surfaces with micro-grooves in a series of experiments, with the groove depth of 45 (μm), the width of $50-225$ (μm) and the period of $100-250$ (μm). As another example, Tsai *et al.* (2009) have conducted flow experiments in a channel with transverse groovy SH walls, in which the groove width, depth and period have been 16 (μm), 20 (μm) and 27 (μm), respectively. In the study of Ou & Rothstein (2005), the groove width, depth and period have been $20-120$ (μm), 25 (μm) and $40-150$ (μm), respectively. On the other hand, Song *et al.* (2018) have used millimetre range sizes of the groove geometry in channel flow experiments, where the groove width, length and

depth have been chosen as 1 (mm), 5 (mm) and 5 (mm), respectively. (iii) Considering that the groove period can vary from tens of micrometers to several millimetres, for the thin to thick channel limits, the half channel height $(\hat{H})$ can also possess a wide range of values, from micrometers to centimetres. Finally, the average flow velocity $\hat{U}_{ave}$ can have a wide range of values as well.

Considering the discussion above, the Reynolds number can vary in the wide range of $10^{-4} \lesssim Re \lesssim 10^4$ (or even larger). The Bingham number can also cover the wide range of $10^{-4} \lesssim Bi \lesssim 10^4$. In addition, based on the possible sizes of the groove period and the half channel height, ℓ can also have the wide range of $10^{-3} \lesssim \ell \lesssim 10^1$. Also, the slip area fraction (φ) varies between zero (no-slip) and unity (full-slip). In addition, based on the slip law and the definition of the slip number, we can crudely show that $\frac{\hat{\varepsilon}}{\hat{H}} \approx \frac{\hat{\mu}_a}{\hat{\mu}_p} \frac{\hat{u}_s}{\hat{U}_{ave}} \frac{1}{Bi+C_1}$, which based on typical values of the flow parameters can vary in the range of $10^{-7} \lesssim \frac{\hat{\varepsilon}}{\hat{H}} \lesssim 10^{-3}$. Remind that $\hat{\varepsilon}$ is the average characteristic distance in the air layer where the air velocity reaches zero. Note that $\hat{\varepsilon}$ does not represent the groove depth; in fact, considering the air flow inside the groove conceptually similar to a lid-driven flow, the distance $\hat{\varepsilon}$ (which can be linked to the liquid/air interface distance from the center of the lid-driven vortex) should be smaller than the groove depth. Finally, based on the range of $\frac{\hat{\varepsilon}}{\hat{H}}$, the range of $b = \frac{\hat{b}\hat{\mu}_p}{\hat{H}}$ can be found as $10^{-5} \lesssim b \lesssim 10^1$.

6. Plane Poiseuille flow of a Bingham fluid with homogeneous slip at the lower wall

Here, we solve for the velocity profile of plane Poiseuille flow of a Bingham fluid, assuming the Navier slip law at the lower wall and the no-slip condition at the upper one. This problem has been already addressed by Panaseti & Georgiou (2017); however, we re-drive the solution in the form of our dimensionless parameters and, eventually, find a simplified closed form relation for the critical slip number at which the lower yield surface reaches the lower wall, *i.e.* $h = 0$. Solving the momentum balance equation, the following relation for the velocity field is obtainable:

$$U(y) = \begin{cases} \frac{G}{2}y^2 + (\tau_w - Bi)\, y + b\tau_w, & 0 \leqslant y \leqslant h, \\ \frac{G}{2}h^2 + (\tau_w - Bi)\, h + b\tau_w, & h \leqslant y \leqslant h^u, \\ \frac{G}{2}y^2 + (\tau_w + Bi)\, y - 2\,(G + \tau_w + Bi)\,, & h^u \leqslant y \leqslant 2, \end{cases} \tag{S17}$$

where $G = \partial P/\partial x$ and is generally obtained through an iterative procedure considering a continuous velocity profile at the upper yield surface, *i.e.* h^u, and the fixed flow rate. In addition, the location of the lower and upper yield surfaces are obtained as $h = \frac{Bi-\tau_w}{G}$ and $h^u = \frac{-Bi-\tau_w}{G}$, respectively.

At the critical condition, where $h = 0$, we have $\tau_w = Bi$ and there is only one yielded zone, which is the upper yielded zone near the upper wall. Considering the continuity of the velocity profile at the upper yield surface and having the fixed flow rate, the following relation is obtained for the critical slip number:

$$b^h_{cr} = -\frac{1}{Bi}\left(2\frac{Bi^2}{G_{cr}} + 2G_{cr} + 4Bi\right), \tag{S18}$$

where G_{cr} is obtained as:

$$G_{cr} = -\frac{\sqrt[3]{8Bi^3 - 12Bi^2 - 6Bi - 1 + 4\sqrt{-24Bi^5 - 12Bi^4 - 2Bi^3}}}{8} - \frac{(2Bi+1)^2}{8\sqrt[3]{8Bi^3 - 12Bi^2 - 6Bi - 1 + 4\sqrt{-24Bi^5 - 12Bi^4 - 2Bi^3}}} - \left(\frac{2Bi+1}{4}\right) + \frac{1}{2}\left(i\sqrt{3}\left(\frac{\sqrt[3]{8Bi^3-12Bi^2-6Bi-1+4\sqrt{-24Bi^5-12Bi^4-2Bi^3}}}{4} - \frac{(2Bi+1)^2}{4\sqrt[3]{8Bi^3-12Bi^2-6Bi-1+4\sqrt{-24Bi^5-12Bi^4-2Bi^3}}}\right)\right). \quad \text{(S19)}$$

REFERENCES

Akbari, S. & Taghavi, S.M. 2022*a* From breakup to coiling and buckling regimes in buoyant viscoplastic injections. *Journal of Fluid Mechanics* **940**.

Akbari, S. & Taghavi, S.M. 2022*b* Immersed buoyant viscoplastic injections. *Journal of Non-Newtonian Fluid Mechanics* p. 104836.

Balmforth, N.J., Frigaard, I.A. & Ovarlez, G. 2014 Yielding to stress: Recent developments in viscoplastic fluid mechanics. *Annual Review of Fluid Mechanics* **46**, 121–146.

Choi, W., Kang, M., Park, J.Y., Jeong, H.E. & Lee, S.J. 2021 Enhanced air stability of superhydrophobic surfaces with flexible overhangs of re-entrant structures. *Physics of Fluids* **33** (2), 022001.

Eslami, A., Akbari, S. & Taghavi, S.M. 2022 An experimental study of displacement flows in stationary and moving annuli for reverse circulation cementing applications. *Journal of Petroleum Science and Engineering* **213**, 110321.

Eslami, A., Basak, R. & Taghavi, S.M. 2020 Multiphase viscoplastic flows in a nonuniform Hele-Shaw cell: a fluidic device to control interfacial patterns. *Industrial & Engineering Chemistry Research* **59** (9), 4119–4133.

Eslami, A. & Taghavi, S.M. 2017 Viscous fingering regimes in elasto-visco-plastic fluids. *Journal of Non-Newtonian Fluid Mechanics* **243**, 79–94.

Eslami, A. & Taghavi, S.M. 2019 Viscous fingering of yield stress fluids: The effects of wettability. *Journal of Non-Newtonian Fluid Mechanics* **264**, 25–47.

Lyu, S. & Taghavi, S.M. 2020 Viscoplastic displacements in axially rotating pipes. *Journal of Non-Newtonian Fluid Mechanics* **284**, 104353.

Mongruel, A., Chastel, T., Asmolov, E.S. & Vinogradova, O.I. 2013 Effective hydrodynamic boundary conditions for microtextured surfaces. *Physical Review E* **87** (1), 011002.

Ou, J. & Rothstein, J.P. 2005 Direct velocity measurements of the flow past drag-reducing ultrahydrophobic surfaces. *Physics of Fluids* **17** (10), 103606.

Panaseti, P. & Georgiou, G.C. 2017 Viscoplastic flow development in a channel with slip along one wall. *Journal of Non-Newtonian Fluid Mechanics* **248**, 8–22.

Pourzahedi, A., Zare, M. & Frigaard, I.A. 2021 Eliminating injection and memory effects in bubble rise experiments within yield stress fluids. *Journal of Non-Newtonian Fluid Mechanics* **292**, 104531.

Song, D., Song, B., Hu, H., Du, X., Du, P., Choi, C.H. & Rothstein, J.P. 2018 Effect of a surface tension gradient on the slip flow along a superhydrophobic air-water interface. *Physical Review Fluids* **3** (3), 033303.

Taghavi, S.M. 2022 Displacement flows in rotating pipes. *Science Talks* **3**, 100066.

Tsai, P.A., Peters, A.M., Pirat, C., Wessling, M., Lammertink, R.G.H. & Lohse, D. 2009 Quantifying effective slip length over micropatterned hydrophobic surfaces. *Physics of Fluids* **21** (11), 112002.

Vasudevan, M. 2017 Implementation of partially slip boundary conditions. *In Proceedings of CFD with OpenSource Software* .